

## Chapter 5

# Understanding Geometric Bias in Crater Counts

### 5.1 Introduction

The size-frequency distribution of craters on a planetary surface is a key measurement in quantifying certain properties of that surface, including its relative age as well as the size distribution of impactors responsible for creating it. In particular, the Moon has remained an important object of study in this respect both because its relative proximity allows for detailed examination of the surface by ground observers and spacecraft and because its heavily cratered surface provides a natural laboratory for examining a range of impact processes and radiometric dating of returned Apollo samples provide an absolute calibration for the timescale. Furthermore, understanding the crater distribution on the Moon provides crucial information as to the impactor flux on other planetary bodies, allowing for correlation of geological epochs across the solar system. As such, the distribution of craters on the lunar surface has been the topic of considerable attention by researchers throughout the twentieth century, especially in the decades following the return of the first images obtained by orbiting spacecraft, the preparation of geological maps of the Moon, and subsequent lunar missions returning image and topography data at ever higher resolution and precision (*Hartmann, 1985; Chapman and McKinnon, 1986; Melosh, 1989; Ivanov et al., 2002; Neukum et al., 2001; Richardson, 2009*).

Many measurements of the size-frequency of lunar craters have been made throughout the last

few decades (*Neukum et al.*, 2001; *Ivanov et al.*, 2002), almost always by human researchers identifying crateriform structures by eye, and crater counting remains an important tool for planetary scientists. However, translating between the distribution of currently visible craters and the underlying distribution of craters that were actually emplaced may not be entirely straightforward. For example, *Robbins et al.* (2014) describes recent work to integrate results from the citizen science project CosmoQuest Moon Mappers (<http://www.cosmoquest.org>), which allows members of the public to contribute to crater counts on the lunar surface using high-resolution images from the Lunar Reconnaissance Orbiter Camera (LROC). Comparison of expert and non-expert crater counts shows that while the derived crater distributions overlap, variability among the features identified is large, even among experts using a variety of software tools and methods. No two people will identify the same set of circular features in an image, especially in dense regions where crater overlap is common (*Robbins et al.*, 2014). At the same time, automated crater identification is numerically challenging, particularly on real surfaces containing traces of multiple geologic processes, and cannot yet compete with human observations in terms of accuracy. Understanding the statistical variations among crater counters, as well as the systematic biases affecting them, is therefore essential in order to further quantify lunar size-frequency distributions useful for relative age dating of surfaces and constraints on the impactor population responsible for producing them.

One such systematic bias was first noted by *Mullins* (1976) in his analysis of the stochastic crater model proposed and subsequently elaborated by *Marcus* (1964), *Marcus* (1966c), *Marcus* (1966b), *Marcus* (1966a), *Marcus* (1966d), and *Marcus* (1967), in which an assumption of non-saturation conditions had to be made in order to successfully analyze the statistics of the crater distribution (*Mullins*, 1976). In particular, *Marcus* (1964) derives an estimate of crater density as a function of time for pristine craters, those whose rims are completely intact, while *Marcus* (1966c) attempted to treat craters for which any portion of the rim is visible, but effectively had to limit his analysis to regions of little to no overlap to solve the equations. As *Mullins* (1976) points out, the choice of criterion determining which features are “visible” in regions of significant overlap has a large effect on the resulting size-frequency distribution of craters because large craters tend to be overcounted

compared to small ones. This geometric bias was explored further by *Woronow* (1978), who used a numerical model to track rim points through time, although his model was criticized by *Chapman and McKinnon* (1986) because it used only 8 rim points to define each crater and could accommodate a dynamic range in crater sizes of only 16. Subsequent work (*Woronow*, 1985a,b) addressed these concerns and confirmed the existence of the geometric bias.

The cratered terrain model developed in the previous chapter has a rim-tracking feature that allows it to account for the surviving rim fragments of each emplaced crater through time for a large number of rim points and range of crater sizes (Fig. 5.1). This chapter first explores this numerical approach, then compares the results to those of *Mullins* (1976), *Marcus* (1964), *Marcus* (1966c), and *Woronow* (1985b), and finally assesses the implications for current crater counting efforts on the Moon and other planetary bodies. Our approach improves upon the previous works described in several respects, most notably in that it tracks the 3-dimensional evolution of the topography simultaneously with the surviving rim segments of each crater emplaced, and applies considerably greater computing power to maximize both the dynamic range of craters used and the resolution of each crater’s rim.

## 5.2 Criteria for “Visible” Craters

The human eye is adept at identifying craters, even when they overlap or are otherwise partially obscured. Nevertheless, there are some limits beyond which a degraded crater cannot be recognized as such by a human researcher. These limits are likely a combination of many factors, including the remaining rim fraction and the connectedness of rim arcs, and may differ depending on dataset properties such as illumination angle, resolution, and the availability of topographic information. There is no consensus opinion among researchers on the ideal criterion for defining the “visibility” of craters on a model-generated terrain. *Mullins* (1976) and *Woronow* (1985b) choose the remaining rim fraction as a proxy for crater survival, whereas *Richardson* (2009) tracks the area of each emplaced crater through time, factoring in destructive processes such as infilling by slope failure and regolith gardening in addition to crater overlap. Because the rim itself is essential both to identifying

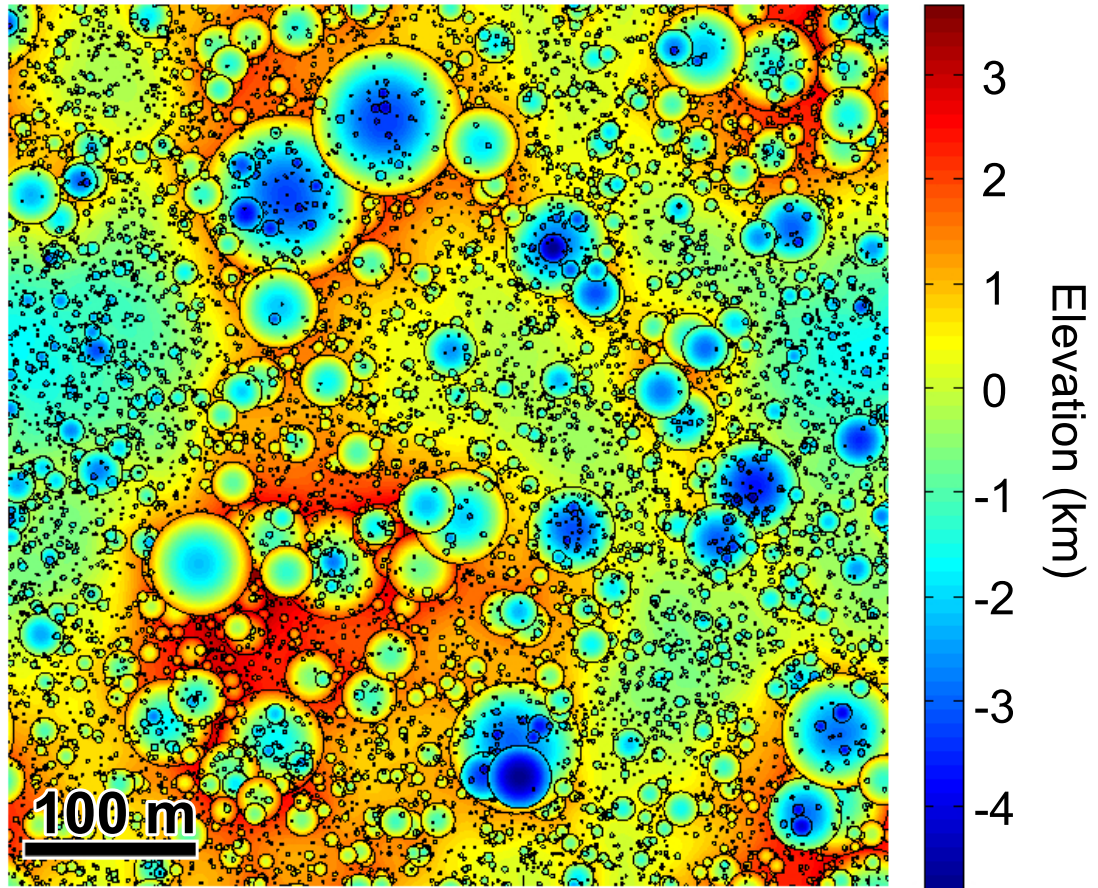


Figure 5.1: Sample topography (color scale) generated by the cratered terrain model described in the previous chapter with surviving rim fragments overlain (black).

craters—due to the sharp relief it provides in images and to the unique circular character it displays—and to measuring their diameters, we follow the former approach. This choice is supported by *Robbins et al.* (2014), in which several crater experts discussed using the sharp, circular transition from light to dark to identify craters. The fraction  $f_{\text{vis}}$ , ranging from 0 to 1, is defined as the minimum fraction of rim remaining such that a crater can be classified as “visible.” Fresh craters are pristine, with  $f_{\text{vis}} = 1$ , and over time this value decreases as subsequently-emplaced overlapping craters remove all or part of the rim. Craters with rim fractions less than  $f_{\text{vis}}$  are deemed “invisible” and are thus discounted in the resulting size-frequency distribution.

## 5.3 Cratered Terrain Model

### 5.3.1 Rim Tracking

The cratered terrain model introduced in the previous chapter emplaces craters on a flat plane with diameters selected according to a cumulative size-frequency distribution:

$$N_{\text{cum}} \propto D^{-\alpha}, \quad (5.1)$$

where  $N_{\text{cum}}$  is the number of craters greater than or equal to diameter  $D_A$ , and  $\alpha$  is the size-frequency distribution exponent. While observed size-frequency distributions of lunar craters are more complicated than a single power law (*Neukum et al.*, 2001; *Ivanov et al.*, 2002), they can often be treated as piecewise power law segments in specific diameter ranges. Understanding the fundamental effects of overlap in this simplified case can therefore provide useful insights into more complex distribution functions as well.

Each incoming crater is assigned a diameter, a random location, and a set of rim points that are tracked throughout the remainder of the simulation. The number of rim points can be specified in two ways, either by fixing the spacing between rim points or fixing the number of points defined for each crater directly. The former method allots more rim points for larger craters than smaller ones, and the spacing is therefore determined by the circumference of the smallest crater included in

the model, of diameter  $D_{\min}$ . Directly fixing the number of rim points per crater allows for greater precision in rim fraction for the smallest craters, but adds a very large number of points to the total simulation, requiring additional computation time. The fixed rim point spacing method is therefore preferred, with the provision that the minimum number of points per crater be sufficient to resolve the surviving rim fragments of the smallest craters. No fewer than 30 rim points were used for any craters in these simulations.

As subsequent craters overlap and obliterate an existing crater, an algorithm determines which previously-existing rim points fall within the polygon defined by the rim of the new crater, and these are removed from the simulation. For each crater, the fraction of rim remaining unscathed is easily tracked as a function of time, where “time” is parameterized as the number of craters that have been emplaced. Figure 5.1 shows an example of topography generated by the cratered terrain model with the surviving rim fragments of the emplaced craters overlain as black ring segments. The stratigraphic relationships between craters emplaced at earlier and later times are clearly visible in the interrupted arcs and complete circles, respectively.

Once a value for the criterion  $f_{\text{vis}}$  is selected, a size-frequency distribution of “visible” craters can be computed at any given time during the model run. A low value of  $f_{\text{vis}}$  equates to a loose criterion for visibility—only a small portion of the rim need be present to identify the crater and include its diameter in the size-frequency distribution. A high value, on the other hand, denotes a strict criterion; most of the crater rim must be extant in order to identify it.

### 5.3.2 Erasure by Ejecta Emplacement

One criticism of *Woronow* (1978) concerned the lack of ejecta effects in his model (*Chapman and McKinnon*, 1986). Crater rims may be erased by superimposed ejecta as well as direct obliteration by overlap. To address this issue, *Woronow* (1985a) employed two ejecta schemes, one of which increased the effective diameter of each incoming crater when considering rim erasure, and the other of which calculated the thickness of an exponentially-decaying ejecta blanket in order to identify obscured rim points. He found that the two models produced results in good agreement when the

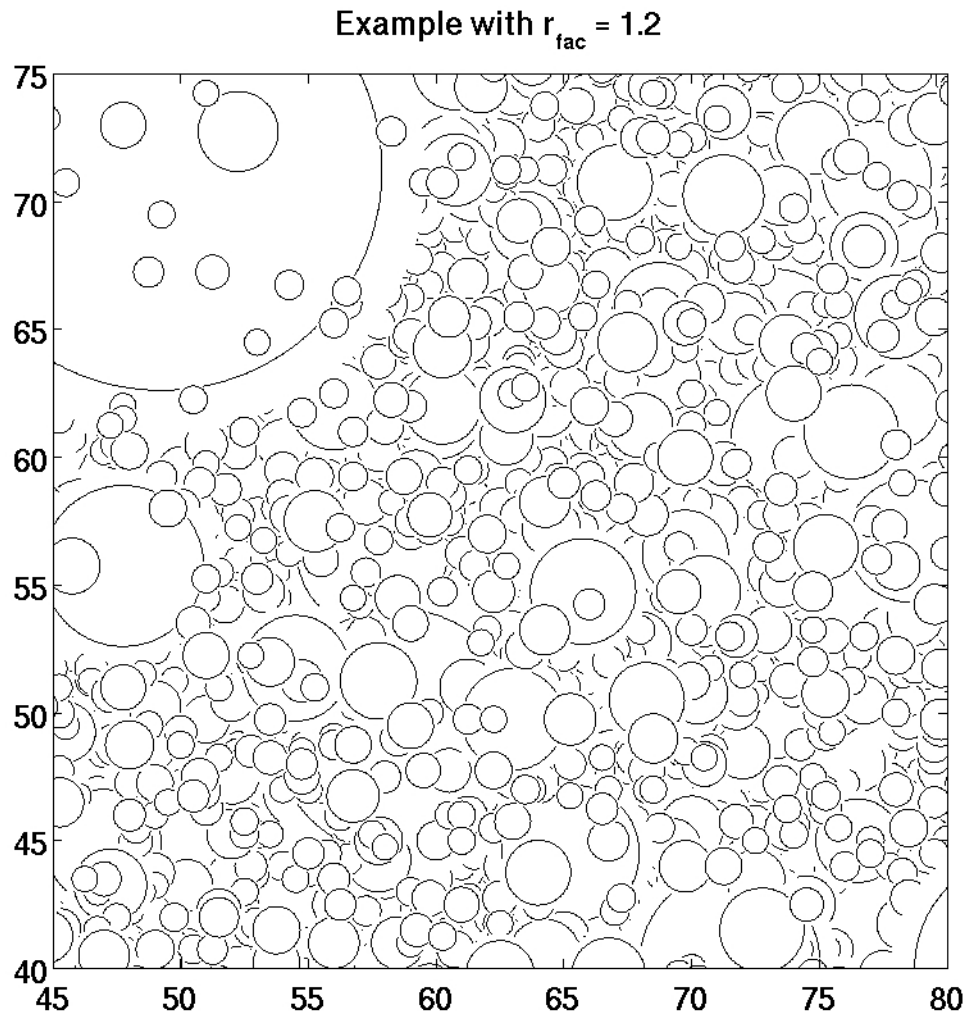


Figure 5.2: Portion of a model terrain showing overlapping rim fragments with  $r_{\text{fac}} = 1.2$ . Each incoming crater erases a circular area with a diameter 20% larger than the crater diameter.

diameter of an incoming crater of size  $D$  was increased by a factor of  $1.1D$  for the purposes of rim erasure. The cratered terrain model presented here also allows for adjustments in this manner, using the multiplicative parameter  $r_{\text{fac}}$  to control the extent of erasure beyond the emplaced crater rim. A value of  $r_{\text{fac}} = 1$  reverts to the “cookie-cutting” case described thus far, while higher values indicate the extent of the ejecta blanket’s capacity to obscure rim points of pre-existing craters. For example, a crater of size  $D = 10$  km with  $r_{\text{fac}} = 1.2$  will remove rim points within 6 km of the crater center while adding its own rim points in a ring 10 km in diameter. Figure 5.2 shows a portion of a simulation using  $r_{\text{fac}} = 1.2$ . An annulus with diameter 20% larger than the crater diameter extends around each new feature, clearly illustrating the difference between the area erased and the rim points added.

## 5.4 Model Results and Observations

### 5.4.1 Craters of One Size

Simulations were first performed with identical craters of diameter  $D_A$  to illustrate the effect of choosing different values of  $f_{\text{vis}}$ , before turning to the more complicated case including many crater sizes. This case is described theoretically by *Melosh* (1989), based in part upon sandbox experiments performed by *Gault* (1970) with a variety of projectiles and explosives. In the latter study, *Gault* (1970) defines the concept of geometric saturation, equivalent to the density of craters achieved in a hexagonal closest-packing arrangement with no overlap. This configuration results in a number density of

$$N_s = 1.15D^{-2}. \quad (5.2)$$

Equivalently, 90.5% of the surface area is covered by craters in the closest-packing arrangement. As the surface accumulates randomly-placed craters, they will overlap each other, and the fraction of area ever covered by at least one crater will increase, surpassing 90.5% at a somewhat higher crater density than  $N_s$  due to overlap:

$$N_{90.5\%} \sim 2.6N_s. \quad (5.3)$$

At this point, which *Gault* (1970) terms the “saturation time,” the number density of observable craters departs from the production function and the surface approaches equilibrium: any incoming crater of size  $D_A$  will, on average, erase an existing crater of that size. The number density of craters thus increases approximately linearly from zero until an equilibrium value is reached, and then remains constant with small fluctuations depending on the arrangement of overlapping craters at any given time.

Crater densities for different choices of  $f_{\text{vis}}$  are presented in Figure 5.3 for a model using only craters with diameter  $D = 20$  km on a domain of size  $X = 128$  km. The density at geometric saturation for this diameter is  $N_s = 0.0029$ , and this value is marked in the figure. In general, crater density behaves as expected, increasing linearly at the beginning of the simulation and leveling to a constant approximately when 90.5% of the the domain is first completely covered by craters. For this simulation, the saturation time (in terms of number of craters emplaced) can be calculated as:

$$N_{90.5\%}X^2 \sim 2.6 \cdot 1.15D^{-2}X^2 \sim 123 \text{ craters}. \quad (5.4)$$

After one saturation time, the number density of craters fluctuates around an equilibrium value, dropping abruptly when large craters clear a broad area and climbing again as smaller craters accumulate.

As is clear from Figure 5.3, the choice of  $f_{\text{vis}}$  has a significant influence on the equilibrium crater density. Using the lowest value shown,  $f_{\text{vis}} = 0.1$ , results in a final density nearly 2.5 times that at geometric saturation. With such a loose criterion for “visibility,” many more overlapping craters can be included than in a closest-packing configuration. On the other hand, using the strictest criterion,  $f_{\text{vis}} = 1$  (pristine craters), reduces the crater density by an order of magnitude. The equilibrium crater density remains below geometric saturation only for values of  $f_{\text{vis}} > 0.4$ . These differences in crater density are easily seen in Figure 5.4, which highlights “visible” craters (shown in blue) on the

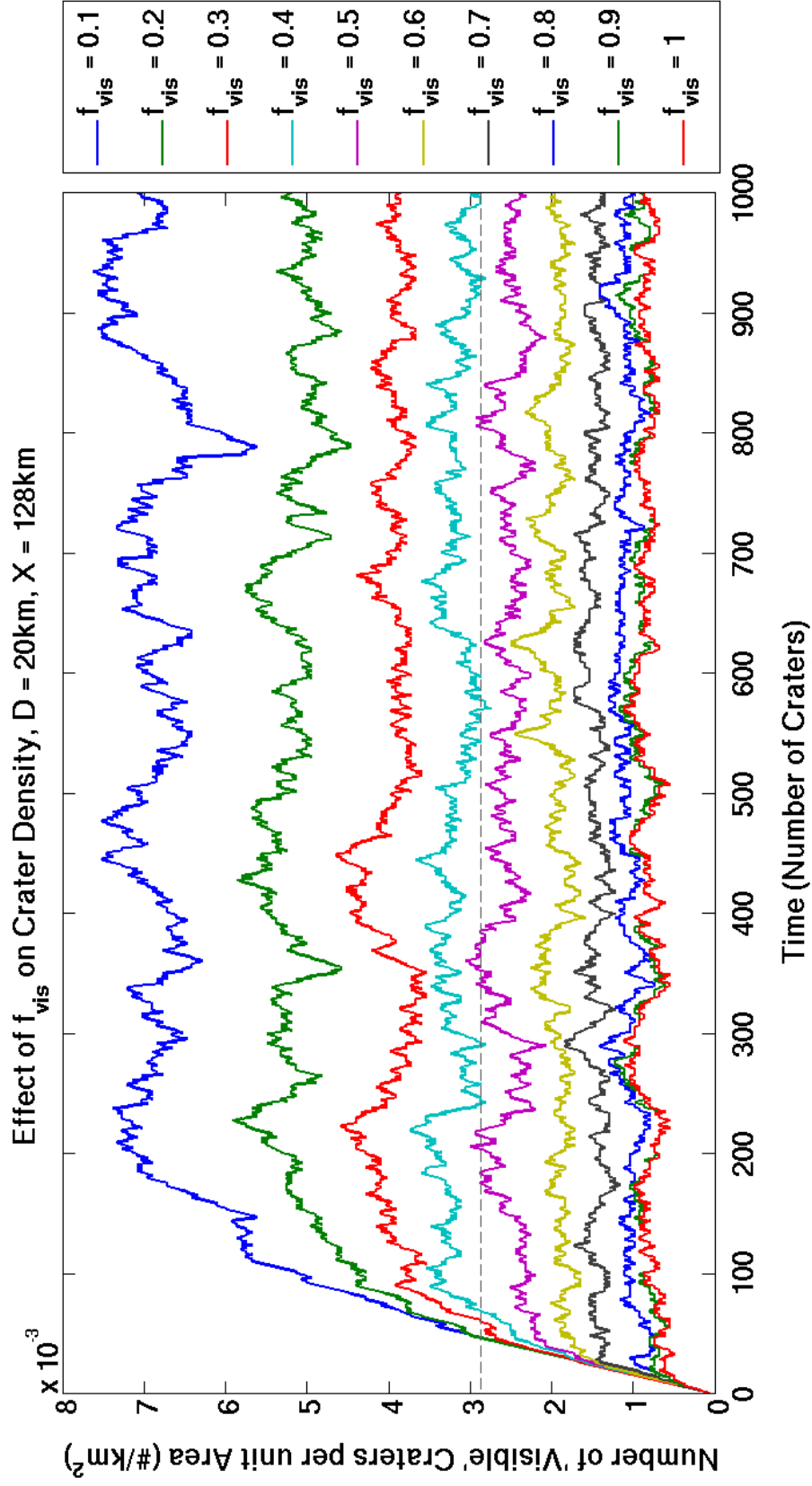


Figure 5.3: Crater density as a function of time (craters employed) for different choices of the criterion for “visible” craters,  $f_{\text{vis}}$ . The domain size is  $X = 128$  km and all craters are of diameter  $D = 20$  km.

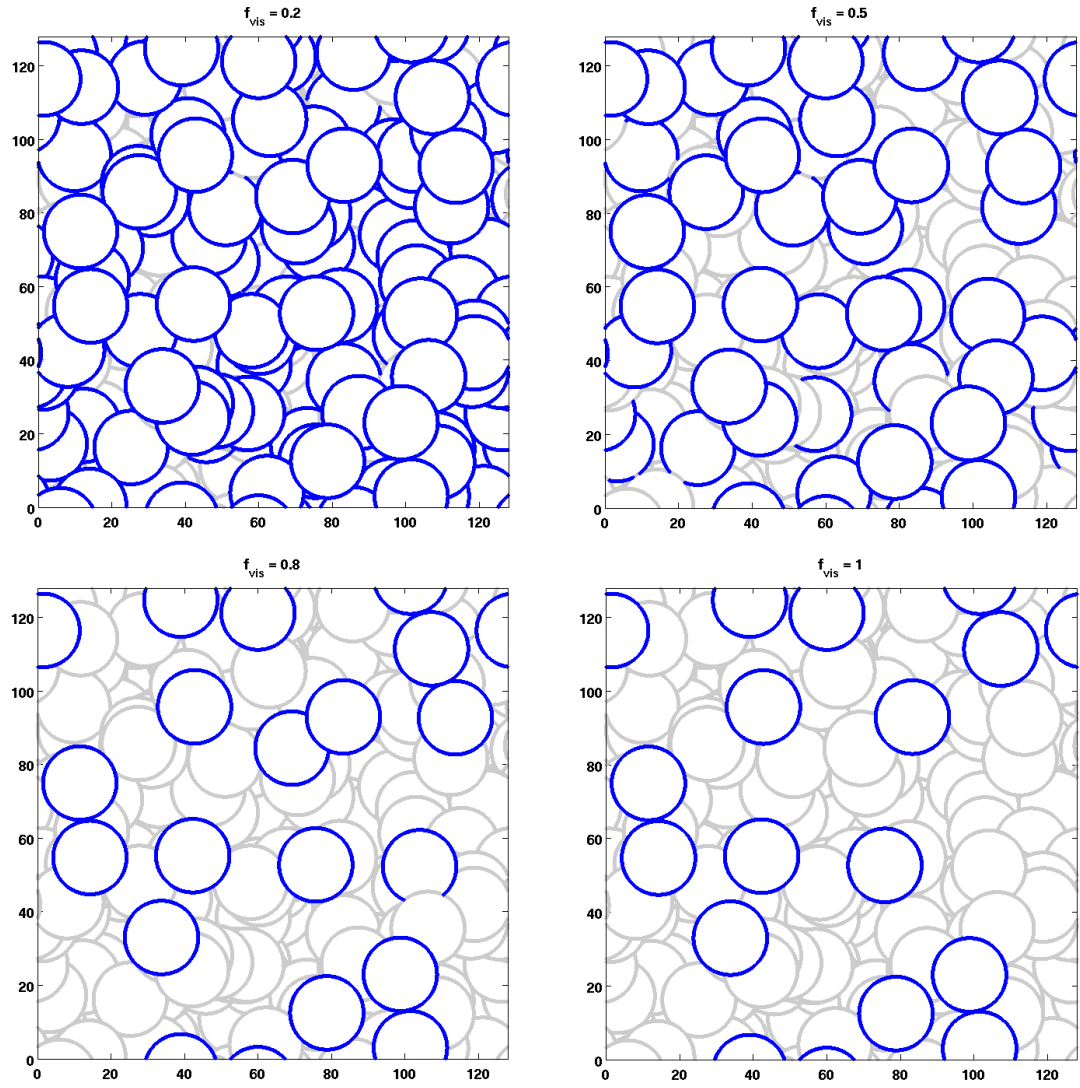


Figure 5.4: Surviving rim points for the single-size crater simulation (gray) highlighting “visible” craters for different values of  $f_{\text{vis}}$  (blue).

same domain for several different values of  $f_{\text{vis}}$  against a background of all surviving rim fragments (shown in gray).

The simulations shown in Figures 5.3 and 5.4 were run in “cookie-cutting” mode, with  $r_{\text{fac}} = 1$ . As expected, increasing  $r_{\text{fac}}$  reduces the crater density for all values of  $f_{\text{vis}}$ , as every new crater is able to erase a larger area than the footprint bounded by the rim. For  $r_{\text{fac}} = 1.2$ , crater density remains below geometric saturation for values of  $f_{\text{vis}} > 0.2$ , and the pristine-crater case ( $f_{\text{vis}} = 1$ ) yields an equilibrium crater density of approximately 20% that at geometric saturation. That the lowest equilibrium densities modeled here are still much greater than the observed crater densities on planetary surfaces indicates that other erasure processes are also important in modifying crater distributions. For this reason, the term *equilibrium* is often used specifically to take into account the interaction of all geologic processes, while *saturation* is used to refer to the impact cratering process alone.

#### 5.4.2 Multiple Crater Sizes: Geometric Bias

For a given production function of craters (characterized by size-frequency distribution exponent  $\alpha$  according to Equation 5.1), varying the value of  $f_{\text{vis}}$  between 0 (the most relaxed criterion) and 1 (the strictest) results in significant variation in the slope of the measured size-frequency distribution,  $\alpha'$ . Smaller values of  $f_{\text{vis}}$  result in a shallower size-frequency distribution (smaller  $\alpha'$ ), while large  $f_{\text{vis}}$  result in large  $\alpha'$ . An example of this behavior for a production function with  $\alpha = 1.5$  is shown in Figure 5.5. The black dashed line indicates the power law exponent of the production function ( $\alpha$ ), which only coincides with the observed size-frequency distribution slope ( $\alpha'$ ) for values of  $f_{\text{vis}}$  between  $\sim 0.4$  and  $0.5$ .

This behavior can be understood by considering the range of rim fractions that survive at any given moment within one crater size bin. Given an existing crater  $A$  of size  $D_A$ , incoming craters with randomly chosen centers will either overlap with  $A$  or miss it entirely. Assuming that new crater  $B$  of size  $D_B$  overlaps with  $A$  by some amount, there are two possible outcomes: either the new crater obliterates a section of the old crater’s rim, or it covers the old crater entirely (if  $D_B > D_A$ ).

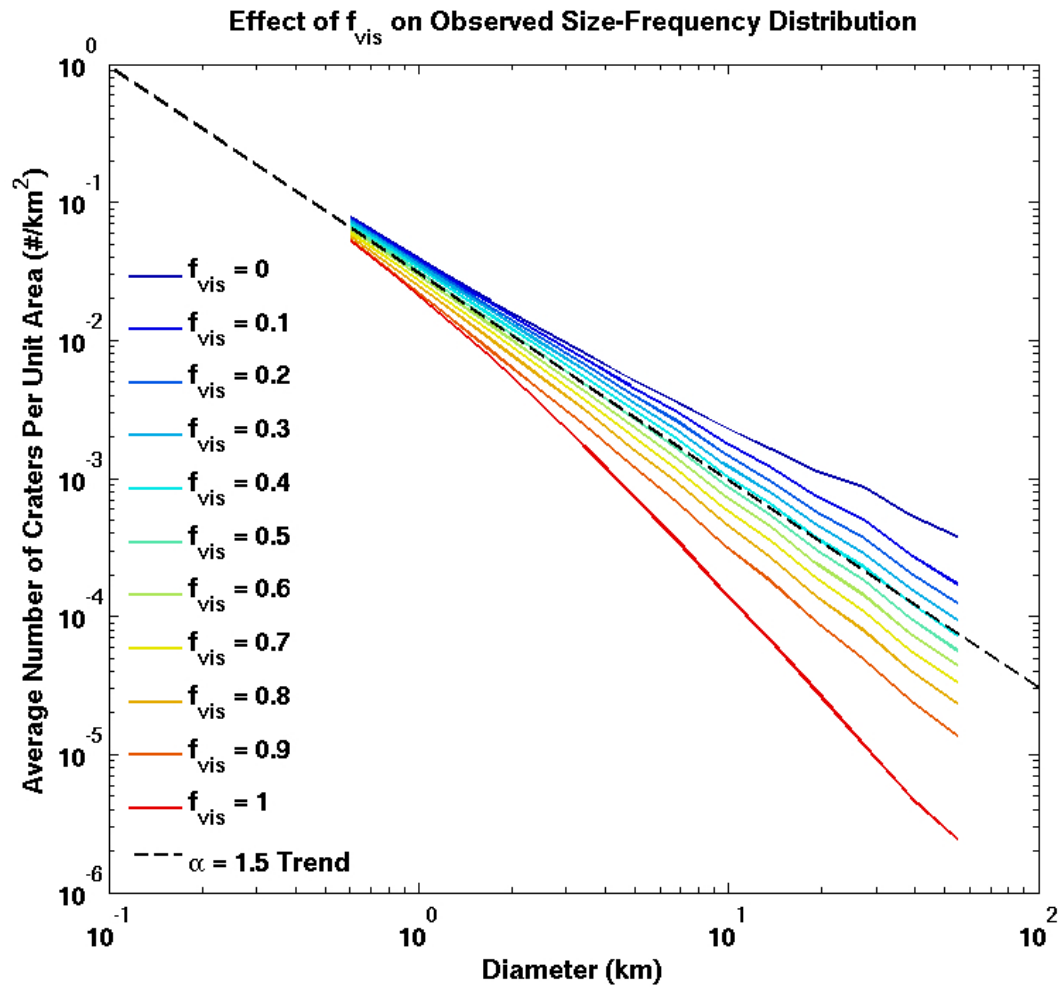


Figure 5.5: Observed size-frequency distribution as a function of  $f_{\text{vis}}$  for a simulation using  $\alpha = 1.5$ ,  $D_{\text{min}} = 500$  m,  $D_{\text{max}} = 64$  km, and  $X = 128$  km. The black dashed line indicates the slope of the production function ( $\alpha = 1.5$ ), which coincides with the observed slope ( $\alpha'$ ) only for  $0.4 < f_{\text{vis}} < 0.5$ .

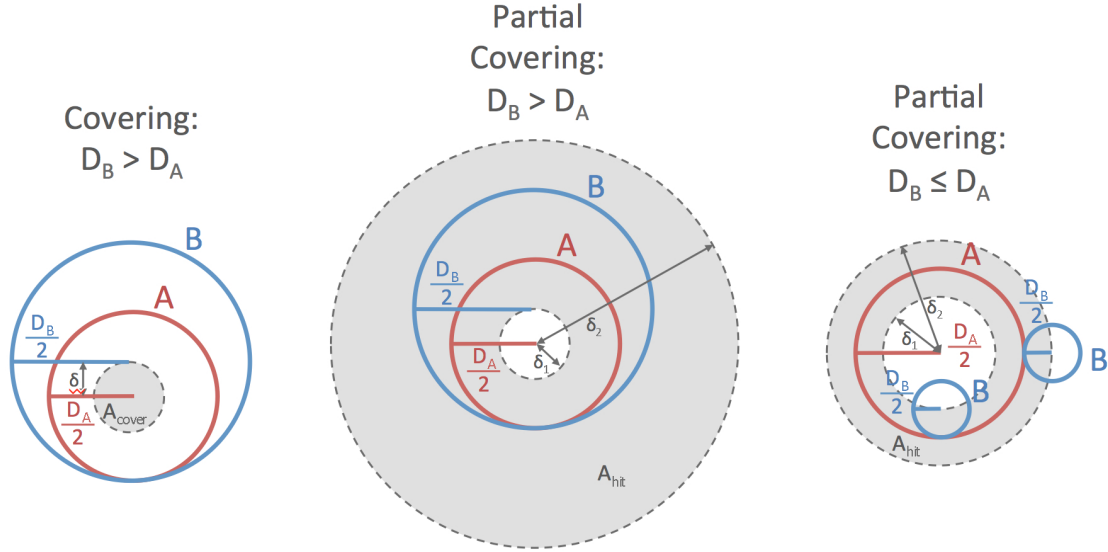


Figure 5.6: Assuming that new crater  $B$  overlaps by some amount with existing crater  $A$ , it will either cover it completely or erase only part of the rim, depending on where crater  $B$  falls in relation to  $A$ . This diagram shows the areas  $A_{\text{cover}}$  and  $A_{\text{hit}}$  within which the center of  $B$  must fall to entirely erase or partially cover  $A$ , respectively, for the two cases where the diameter of  $B$  ( $D_B$ ) is larger or smaller than that of  $A$  ( $D_A$ ).

The outcome is determined by where crater  $B$  falls in relation to crater  $A$ . There is a certain area,  $A_{\text{cover}}$ , within which crater  $B$  will always cover crater  $A$ . Another area exists,  $A_{\text{hit}}$ , within which crater  $B$  will cover part, but not all, of the rim of crater  $A$ . These areas are illustrated in Figure 5.6 and can be written as follows:

$$A_{\text{cover}} = \begin{cases} \pi \left( \frac{D_B}{2} - \frac{D_A}{2} \right)^2 & D_B > D_A \\ 0 & D_B \leq D_A \end{cases} \quad (5.5)$$

$$A_{\text{hit}} = \pi D_A D_B. \quad (5.6)$$

Thus, assuming that crater  $B$  overlaps crater  $A$  by some amount, the probability that it will cover the pre-existing crater completely is related to the ratio of these areas and the probability that crater  $B$  is of a given size  $D_B$ . For most crater sizes,  $A_{\text{cover}}$  is larger than  $A_{\text{hit}}$ ; only craters with diameters near or less than  $D_A$  are more likely to partially cover crater  $A$  than erase it (Fig. 5.7). According to Eqn. 5.1, however, small craters are much more likely to occur than large craters, since

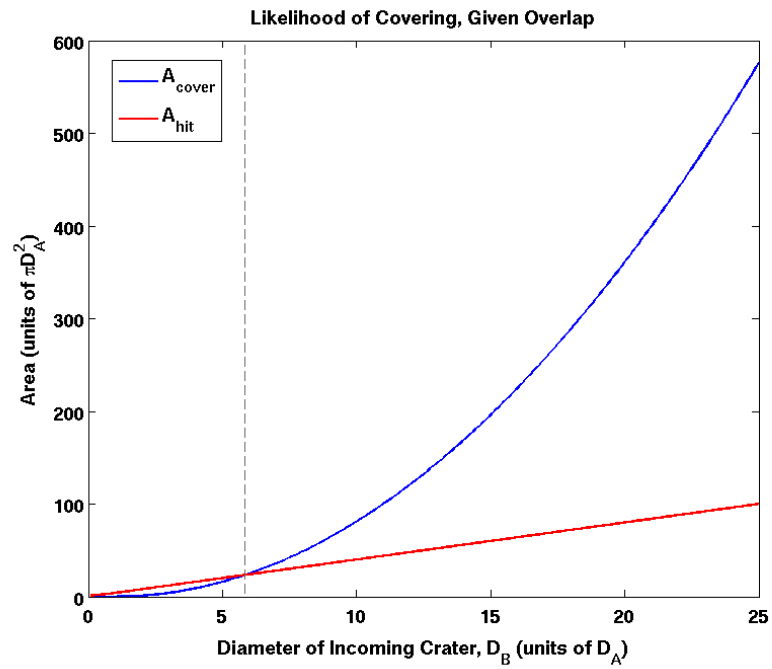


Figure 5.7: The areas  $A_{\text{cover}}$  and  $A_{\text{hit}}$  as a function of  $D_B$ , the size of the incoming crater  $B$ . Assuming that some overlap occurs, if  $D_B$  is smaller than  $\sim 6D_A$ , it is slightly more likely that a randomly-placed crater  $B$  will partially cover  $A$  than completely cover it (for  $D_B < D_A$  complete covering is impossible). For larger  $D_B$ , it becomes increasingly more likely that  $B$  will entirely cover  $A$ .

$\alpha$  is always positive. Together, these constraints create variation in the distributions of surviving rim fractions across different crater sizes. Large craters are unlikely to be hit by craters larger than themselves because they are rare, and very likely to be hit by abundant small craters. Therefore, one would expect that at any given time, few large craters survive with a large fraction of their rims intact.

Small craters, on the other hand, are more likely to be hit by craters larger than themselves, and therefore much more likely to be covered completely than large craters. Thus, we would expect to find that most surviving small craters have large rim fractions remaining, because those that are hit at all are usually completely erased. Intermediate crater sizes should transition between the two end cases. Examination of the distribution of rim fractions within crater diameter bins bears out these expectations. Small craters that have not been completely erased are more likely to have large surviving rim fractions, while the opposite is true for large craters. Exceptions to this rule occur at the very largest rim fractions, where recently-emplaced craters of all sizes have not had much opportunity to be hit by subsequent craters, and at the very smallest rim fractions, where small rim fragments have avoided final erasure because they occupy a small fraction of the domain and are thus unlikely to be hit.

Using incremental values of  $f_{\text{vis}}$  and taking into account uncertainties in the linear fits, the relationship between  $\alpha'$  and  $f_{\text{vis}}$  can be further examined for varying  $\alpha$ , and the results of this analysis are shown in Figure 5.8. If the observed size-frequency distribution were to maintain the slope of the production function, then the curves would be flat for any value of  $f_{\text{vis}}$ . For most of the range of  $f_{\text{vis}}$ , however,  $\alpha'$  increases linearly from approximately  $\alpha' \sim \alpha - 0.25$  to  $\alpha' \sim \alpha + 0.25$ . This linear trend breaks down near  $f_{\text{vis}} = 0$ , where the extremely loose visibility criterion favors large craters, and near  $f_{\text{vis}} = 1$ , where the pristine-crater criterion favors small craters. This amplification of the geometric effects at the extremes of  $f_{\text{vis}}$  is readily apparent in Figure 5.5. As  $\alpha$  increases, the slope of the linear trend decreases, and the effects near  $f_{\text{vis}} = 0$  and 1 become increasingly confined to the edges. Changing the value of  $r_{\text{fac}}$  has little effect on the  $\alpha'$  curves, especially for values of  $\alpha < 2$ .

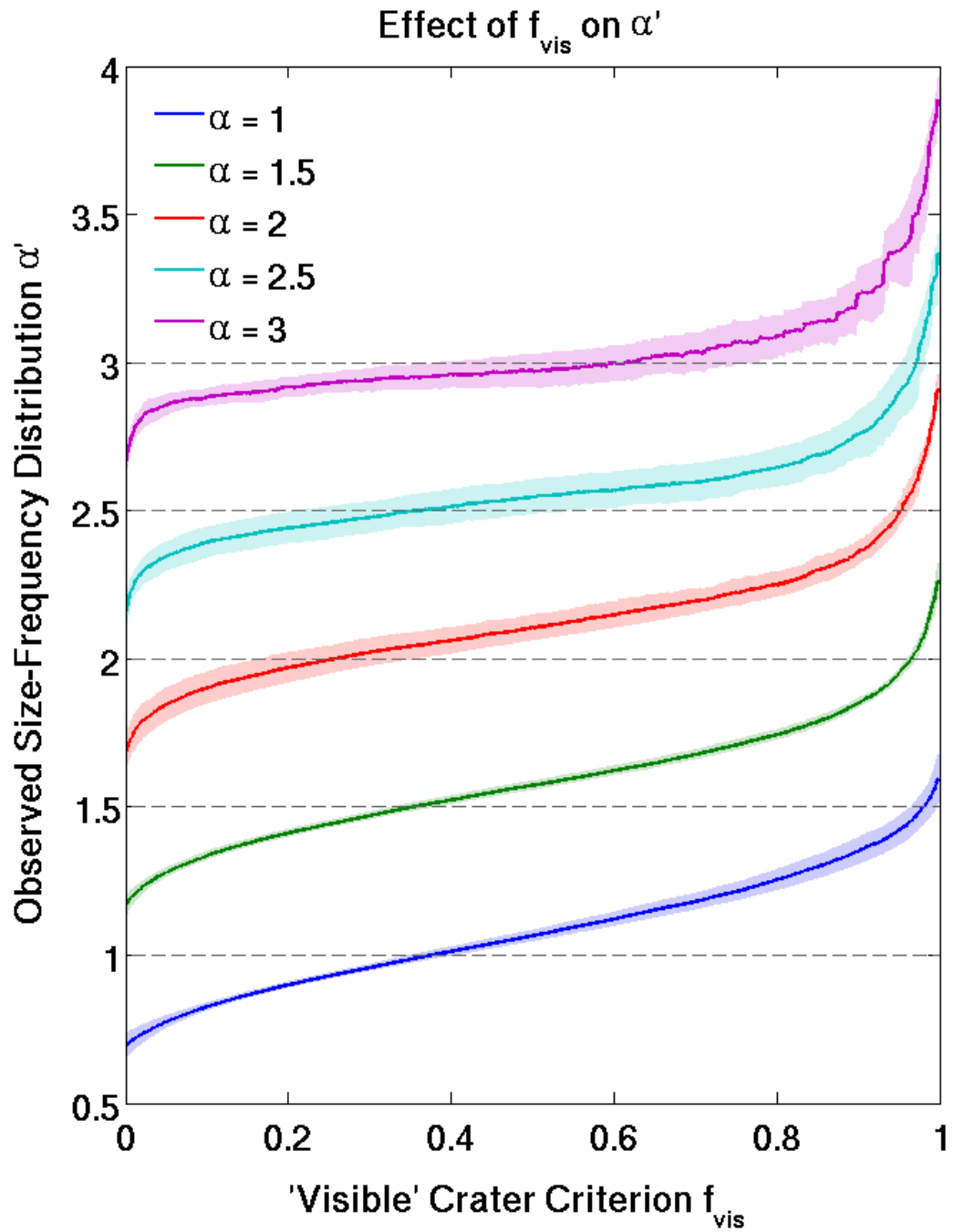


Figure 5.8: Slope of the observed size-frequency distribution ( $\alpha'$ ) for different values of  $f_{\text{vis}}$ , the criterion for visibility, plotted for several production function slopes ( $\alpha$ ).

These results are consistent with those of *Woronow* (1985b), but we extend the range of  $f_{\text{vis}}$  considered and improve considerably the precision of the calculation applied to the problem. The geometric bias first noted by *Mullins* (1976) is clearly present, with large craters being overcounted at small  $f_{\text{vis}}$  and undercounted at large  $f_{\text{vis}}$ .

### 5.4.3 Potential Corrections

#### 5.4.3.1 Pristine-Crater Criterion

One strategy often used by crater counters to estimate the production function is to classify features by their state of degradation and examine only the size-frequency distribution of the most pristine craters (*Chapman*, 1968; *Chapman et al.*, 1970; *Strom*, 1977). Because these craters represent the most recent features to be emplaced, it is inferred that they most closely reflect the production function. However, as Figure 5.8 shows, the pristine-crater criterion does not produce the best estimate of the underlying size-frequency distribution of emplaced craters because it tends to undercount large craters that are likely to have been partially (but not completely) covered by smaller ones. Using a value of  $f_{\text{vis}} = 1$  thus results in an overestimate of  $\alpha$  by as much as 0.5 to 1, a significant amount considering the detailed crater histories inferred from slight changes in the slope of the size-frequency distribution.

#### 5.4.3.2 Weighting by Rim Fraction

A somewhat better method to correct for the geometric bias in crater counts was suggested by *Mullins* (1976) and *Mullins* (1978) and supported by *Woronow* (1985b). Rather than choosing the most pristine craters, which is equivalent to using  $f_{\text{vis}} = 1$ , *Mullins* (1976) uses a weighted histogram of “visible” craters, where the weights are given by the fraction of rim surviving for each crater. Weighting by rim fraction compensates for the overcounting of large craters at small  $f_{\text{vis}}$ . Figure 5.9 shows this correction applied to the  $\alpha'$  curve for  $\alpha = 1.5$ .

While this method does adjust  $\alpha'$  to match  $\alpha$  at  $f_{\text{vis}} = 0$ , it does not correct the  $\alpha'$  curve for higher values of  $f_{\text{vis}}$ , and for strict visibility criteria it actually exacerbates the bias toward smaller

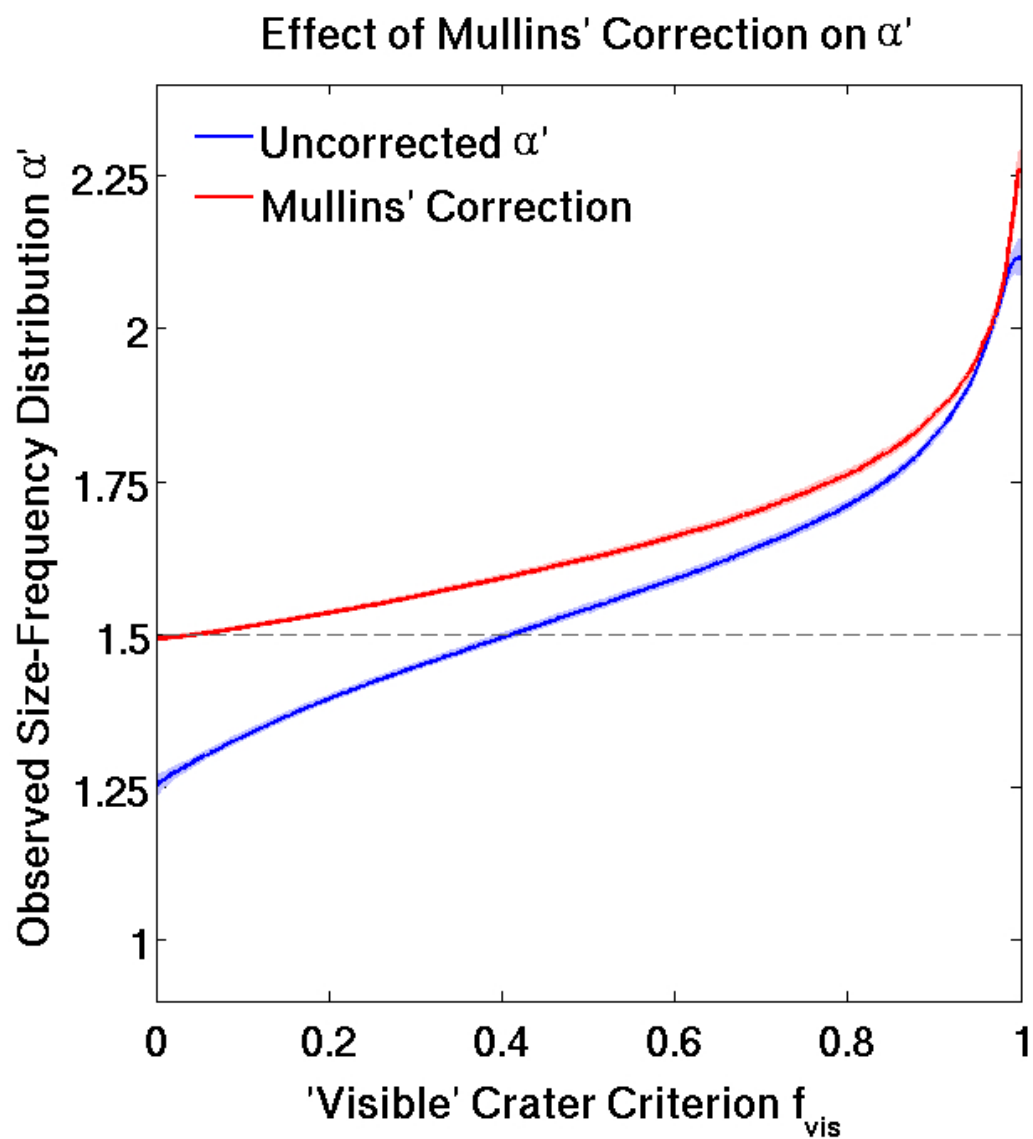


Figure 5.9: Example of the correction proposed by *Mullins* (1976), with  $\alpha = 1.5$ . Histograms of “visible” crater diameters are weighted by the fraction of rim remaining for each crater, compensating for the overcounting of large craters at the smallest values of  $f_{vis}$ .

craters. This correction also introduces logistical issues for human crater counters, for whom it is not trivial to measure the rim fraction of every crater counted, and who cannot be expected to identify craters down to such small remaining rim fractions.

### 5.4.3.3 Personal Visibility Criteria

Each of the curves in Figure 5.8 crosses its respective production function value of  $\alpha$  at some intermediate value of  $f_{\text{vis}}$  between  $\sim 0.3$  and  $0.6$ , implying that these visibility criteria may more accurately reflect the underlying distribution of emplaced craters than others, without further correction. Human crater counters naturally recognize features according to individual and largely subconscious criteria, including (but not limited to) the rim fraction remaining for each crater. Further studies of crater identification methods and outcomes among crater counters, either on model-generated surfaces like those presented here or on actual lunar images like those used by *Robbins et al.* (2014) and CosmoQuest, may provide valuable insights into the fundamental variability of crater counts that can improve future efforts to quantify the Moon’s impact history.

## 5.5 Discussion

The results presented here suggest that interpreting the distribution of craters counted on a planetary surface is not as straightforward as is often presented. Not only is there significant variability between crater counters in the identification of particular features (*Robbins et al.*, 2014), but a geometric bias exists that either under- or overcounts large craters, depending on the criterion used to define “visible” craters. This bias is not mitigated by choosing only the most pristine craters to include in size-frequency distributions. Rather, enforcing this strict criterion for visibility amounts to accepting a value of  $f_{\text{vis}} = 1$ , which actually exacerbates the problem. Using the rim-fraction weighting technique proposed by *Mullins* (1976) compensates for the overcounting of large craters at very low values of  $f_{\text{vis}}$ , but it assumes that crater counters can recognize features when almost all of their rims have disappeared and introduces the requirement that counters record remaining rim fractions for all features they log, further complicating a logistically-intensive and time-consuming

process. A simple solution may be to develop a rule of thumb, where crater counters intentionally reject features with less than  $\sim 0.3$  to  $0.6$  of their rims remaining, roughly corresponding to the range of values of  $f_{\text{vis}}$  where the  $\alpha'$  curves cross their production function values,  $\alpha$ , although this approach does not quantitatively resolve concerns about the comparability of crater counts made by different investigators.

Another possibility would be to investigate the nature of crater recognition itself among human crater counters. Cratered terrain models like the one presented here provide new opportunities to study synthetic terrains for which the exact crater distribution is known, thus allowing for direct quantification of the criteria used to identify features. Our preliminary investigations suggest that the comparison of craters identified on an artificially-illuminated model plane with the known underlying distribution of emplaced craters can provide an estimate of the range of  $f_{\text{vis}}$  implicitly assumed by each crater researcher. However, a comprehensive study is required to address details such as image resolution, minimum and maximum crater sizes, illumination angles, and correlation of emplaced craters with recognized features. The cratered terrain model's ability to track the 3-dimensional topography as well as surviving rim fragments also allows for the quantitative investigation of ejecta effects that can improve our understanding of how rim segments are erased over time.

There is another effect not yet taken into account by the rim-tracking model, which is related to the analysis presented in the previous chapter. The value of  $\alpha$  determines the crater size most efficient at eroding features of any given scale (see Fig. 4.6). When  $\alpha$  is less than 2 (for our 2-dimensional model), large craters dominate the erosion, and they erase all smaller craters simply by covering them. This is also the assumption of the rim-tracking feature: rim points are erased when they fall within  $r_{\text{fac}} \frac{D}{2}$  of the center of a newly-emplaced crater. When  $\alpha > 2$ , however, diffusion (rather than covering) becomes the dominant form of erosion. Using Equation 4.14, the time it takes to diffuse a crater of size  $D$ ,  $t_{\text{diff}}$ , can be estimated. For  $\alpha > 4$ , the smallest craters dominate diffusion of all other scales, and the diffusion time scales as  $D^2$ . Larger craters thus take longer to be erased, and are therefore detectable in the topography even after they have been covered once by smaller craters. Therefore, the 3-dimensional topography contains more information than the rim-tracking algorithm

alone, and, because diffusion times are longer for larger craters, these features may be detectable and their diameters measured even without (or with few) pristine rim segments. As described in the previous chapter (Section 4.3), the equilibrium size-frequency distribution will follow  $D^{2-\alpha}$ . For  $\alpha$  between 2 and 4, each crater size dominates its own diffusion, and the equilibrium size-frequency distribution is independent of  $\alpha$  in this range, with a power law exponent of  $-2$ .

Erosion by diffusion rather than covering requires a redefinition of what it means for a rim point to be erased, and whether a geometric bias continues to exist in this case becomes a complicated question. All craters will be eroded by craters smaller than themselves (in most cases), and the asymmetry in degradation state between small and large craters observed in Section 5.4.2 is therefore expected to be diminished. However, the extent to which crater counters can identify features without sharp rim crests as impact craters is a highly relevant question that remains largely unexamined. The two main processes of erosion—covering and diffusion—produce different expectations for the slope of the equilibrium size-frequency distribution for  $\alpha > 2$ . If rims only need to be covered to be erased, the observed size-frequency distribution will have the same power law slope as the production function (depending on the value chosen for  $f_{\text{vis}}$  and taking into account the geometric bias examined here). If rims need to be diffused to be erased, then the slope of the size-frequency distribution will be  $-2$  regardless of the production function exponent (for  $2 < \alpha \leq 4$ ). Lunar crater counts record a kink in the size-frequency distribution near  $D = 100$  m, above which the power law exponent is  $-2$  and below which it is steeper, suggesting that craters smaller than this size have reached equilibrium and those larger have not (*Soderblom, 1970; Richardson, 2009*). If this is the case, then the diffusive nature of erosion in this range of  $\alpha$  is being detected by crater counters, and they must be identifying features with partially diffused rims. Studies of human crater counters using model-generated terrains may shed light on the complexity of criteria required to recognize degraded craters and measure their diameters.

The large dataset collected by the CosmoQuest Moon Mappers team and summarized by *Robbins et al.* (2014) provides another resource for the quantification of crater identification by many different crater counters. While this dataset lacks the model’s ability to access the real underlying distribution

of craters, it has the advantage of comparing crater counts on the same images among a large number of individuals, providing the opportunity to measure statistical variability among crater distributions. Some observations from *Robbins et al.* (2014) are already of interest to the geometric bias discussed above. For example, crater densities identified by investigators in a Narrow Angle Camera (NAC) image (M146959973L) on a portion of the maria clearly show the effects of crater degradation state on the ability to recognize features. Generally, there are more large degraded craters and more small pristine craters, in complete agreement with the analysis presented here. However, craters counted on highlands terrain in the Wide Angle Camera (WAC) image (M119455712M) show a quite different dependence on degradation state. Large craters that could be identified were more likely to be pristine than small craters, suggesting that large, degraded craters may be difficult to identify on rugged, reworked terrain. The study also mentions that investigators may be more attuned to features near the minimum and maximum crater sizes included in the image (which depend on the image resolution and domain size, respectively), causing them to identify relatively more features at the extremes than at intermediate sizes. This dataset thus represents a valuable means of examining the methods, assumptions, and biases inherent in the process of counting craters on the real lunar surface, and it provides a highly complimentary approach to counting craters on synthetic terrains where the underlying distribution is known.

## 5.6 Conclusions

What does  $f_{\text{vis}}$  represent in practice? For researchers counting craters on a planetary surface, there are inevitable limitations to what the eye can recognize as a crater in a field of overlapping craters, let alone on a surface with multiple geologic processes represented. The fraction of the rim remaining likely plays a role in these limitations, but there are many other factors to consider as well, from how spread out or connected the rim fragments are, to whether there is a size dependence involved. Perhaps counting craters on a topographic map results in a different  $f_{\text{vis}}$  than counting on an image, and certainly factors such as illumination angle and image resolution affect the visibility of partially obscured features. Some of these factors are already taken into account in crater counting—notably

the falloff in small crater populations due to insufficient resolving power. However, the main result of this work—the extent to which we recognize craters may influence our measurements of crater size-frequency distributions—has so far remained largely unexplored. The computing power available to current cratered terrain models, together with the data collected by recent citizen science efforts to map the Moon, provides a new and unprecedented opportunity to address the effect of geometric bias on observed size-frequency distributions on the Moon and throughout the solar system.